

# Relativistic astrospheres of gamma-ray binaries: modeling of non-thermal processes

A. M. Bykov,<sup>1,\*</sup> A. E. Petrov,<sup>1,†</sup> and K. P. Levenfish<sup>1</sup>

<sup>1</sup>*Ioffe Institute, St. Petersburg, 194021 Russia*

A long standing problem in high energy astrophysics is the nature of galactic accelerators of particles with energies above petaelectronvolt (PeV). Such objects are sources of galactic cosmic rays and can produce PeV-regime photons observed by ground-based observatories. Among very likely accelerators are astrospheres of pulsars in gamma-ray binaries. These binaries have long been observed as bright sources of teraelectronvolt (TeV) gamma-ray photons. Recently, 2D relativistic magnetohydrodynamic (rMHD) simulations have shown that the astrospheres can accelerate particles to energies well above PeV, provided that they harbor a Gauss-range magnetic field. Such a strong field is necessary in the region of two colliding winds: the relativistic outflow of the pulsar or accreting black hole and the wind of its stellar companion, a massive early-type star. Here, the wind collision region is explored as the site of PeV protons acceleration. The local structure of colliding flows is illustrated using rMHD simulations of a powerful pulsar wind in 2D and 3D models. The relativistic outflow of a pulsar or black hole, evolving inside the strongly magnetized stellar wind, have an elongated shape and surrounded by a kind of magnetic cocoon providing favorable conditions for acceleration of ultra high energy ions. The simulated spectra of particles, accelerated by intermittent relativistic turbulence in these systems, have piece-wise power-law shape and extend well above PeV energies for powerful outflows. The model indicated that gamma-ray binaries harboring a powerful relativistic outflow, produced either by a pulsar or accreting black hole, can be bright sources of synchrotron MeV-regime photons and multi-PeV regime gamma-rays, as recently detected from galactic microquasars like Cyg X-3. The Gauss-range magnetic field of a massive star wind strongly influences the non-thermal emission of gamma-ray binaries with relativistic companions.

Keywords: MHD simulations, gamma-ray binaries, pulsar wind nebulae

## I. INTRODUCTION

<sup>1</sup> Stellar winds as gas and dust outflows accelerated in the upper atmosphere of stars of various types have long been observed as extended astrospheres [see e.g. 1–4]. More than sixty years of studying the heliosphere with direct measurements of its key physical parameters provided unique information on the dynamics of the solar wind. Detailed models of the heliosphere have been created [5–7], taking into account the kinetics of its multiple components [e.g., 8]. Powerful winds of young massive stars and compact relativistic objects, such as black holes and neutron stars, can also create extended astrospheres visible at many wavelengths.

The winds of neutron stars-pulsars power energetic pulsar wind nebulae, known to be efficient accelerators of wind particles. The accelerated particles can convert up to a few tens of percent of the wind power into non-thermal synchrotron radiation from the nebula, ranging from radio to gamma-rays [9]. This turns pulsar astrospheres into bright synchrotron X-ray sources associated

with sources of very high-energy gamma-rays. Such astrospheres can also produce energetic cosmic-ray (CR) leptons and are plausible antimatter factories that could explain the excess of CR positrons observed in the GeV–TeV range at the Earth orbit [e.g., 10]. Under certain conditions, these objects can also accelerate CR nuclei. Young pulsars with high spin-down luminosity  $\dot{E}$ , such as Crab pulsar, can accelerate particles even to PeV energies [11]. Synchrotron emission of PeV particles falls in the MeV–GeV range if it occurs in magnetic fields of pulsar wind nebulae. This study focuses on the astrospheres of rotation-powered pulsars as accelerators of very high-energy protons.

In binaries where a pulsar orbits a massive early-type star, the pulsar astrosphere may differ from that of an isolated pulsar. Such binaries are characterized by the collision of two flows, the relativistic wind of the pulsar and the powerful wind of its massive companion. The wind collision provides particularly favorable conditions for the efficient acceleration of both leptons and ions. The leptons can emit synchrotron radiation in the strong magnetic field of the system and inverse Compton radiation in the intense radiation field of the massive star [see, e.g. 12]. The hadrons, in turn, can emit gamma-rays by interacting with stellar wind nuclei and with stellar optical/ultraviolet photons [e.g., 13–15]. The systems which appear bright in gamma-rays are called *gamma-ray binaries*; in general, they comprise a compact object (a neutron star or a black hole) and a massive OB star.

\* byk@astro.ioffe.ru

† a.e.petrov@mail.ioffe.ru

<sup>1</sup> This text is a slightly updated version of a review presented at a conference “Cosmic Gas Dynamics” in memory of Professor V.B. Baranov dedicated to the 90th anniversary of his birth, published in Fluid Dynamics v.59, p. 2377, (2024)

The study of gamma-ray binaries is a challenging task, and a number of unsolved problems still present [16]. These include the unknown nature of the compact companion (black hole or pulsar?) in the gamma-ray binaries LS 5039 [17–19] and LSI 61°303 [20, 21], and the uncertainty over which component (leptons or hadrons?) is responsible for the observed gamma-rays, to name a few. Recent observations suggest that gamma-ray binaries might accelerate protons well above PeV. *LHAASO* gamma-ray observatory detected a 1.4 PeV photon from a source in the Cygnus region (which may be associated with the gamma-ray binary PSR J2032+4127) [22]. A sub-PeV gamma-ray flare and neutrino were simultaneously detected from the same region by *Carpet-2* and *Ice Cube* observatories [23].

To solve the above problems it is necessary to model the non-thermal emission of gamma-ray binaries, taking into account the structure of flows in colliding winds. This structure appears to be quite complex, as follows from hydrodynamic (HD) and magnetohydrodynamic (MHD) simulations [see, e.g. 24–29]. Most of the above simulations neglected the effects of the magnetic field of the stellar wind. However, these effects can be important for particle acceleration, especially in short-period or highly eccentric gamma-ray binaries.

To explain the observed sub-PeV flares and neutrinos as produced by protons, the latter must be accelerated above PeV. This requires the presence of a Gauss-range magnetic field in the region of wind collision, as shown by Monte Carlo simulations [15]. Such a strong field can be carried by the wind of O/B/A-type stars, since about 10% of them are found to have surface fields above 100 G [30, 31]. Indeed, the known orbital parameters of observed gamma-ray binaries imply that the orbital separation of their compact and massive companions could range from  $\sim 0.1$  AU to tens of AU, i.e. from units to hundreds of typical radii of massive stars,  $R_* \sim 10^{12}$  cm. Assuming the Parker-type model for the radial structure of the stellar wind ( $sw$ ), with  $B_{sw} \propto R_*/R$ , one would expect  $B_{sw} \sim 0.1$ –10 G in the vicinity of the compact object.

The study of gamma-ray binaries as potential pevatrons is of great interest now. Monte Carlo modeling [15] of these systems was performed under simplified assumptions on the structure of their flows. A more rigorous consideration requires combining relativistic MHD and particle-in-cell (PIC) approaches to describe the dynamics of colliding flows and the propagation of high-energy particles in them, respectively. Such simulations were carried out by Bykov *et al.* [32] in a planar geometry with a limited dynamical range. They studied the local structure of colliding flow in the vicinity of a pulsar, taking into account the strong magnetic field of the stellar wind. A strong field is necessary to keep the accelerating particles inside the accelerator during the time interval they gain energy above PeV. This time interval was shown to be short compared to the orbital period, which justified the local consideration. Whether a planar geometry is

applicable for such a task was a question for study. In this paper we compare results of the planar and full 3D rMHD simulations of gamma-ray binaries that harbor a pulsar. The simulation provided a detailed description of the structure of relativistic flows in these objects and highlight the effect of a strong magnetic field of the stellar wind. We consider the model results in a broad context of the study of non-thermal processes in relativistic astrospheres produced by either young rotation powered pulsar or black hole(or neutron star) accreting at a critical rate.

## II. MHD MODEL SETUP

Self-consistent MHD-PIC modeling of gamma-ray binaries requires resolving their MHD structures on spatial scales smaller than the particle gyroradii,  $R_g$ . For a proton of energy  $\sim 0.1$  PeV in a one-Gauss field, the estimate is  $R_g \sim 0.02$  AU. Meanwhile, the region of colliding flows of interest to us can cover tens of AU. The numerical grid should then have  $\sim 1000$  nodes per dimension to ensure the minimum necessary dynamic range of spatial scales, even if particle acceleration is tracked starting at sub-PeV energies. Starting at lower energies would entail a much higher resolution. The need for a fine grid is compounded by the need to scan the parameter space of the models so that they can provide a realistic description of non-thermal emission of gamma-ray binaries. Such high computational demands on the problem motivate us to look for a more cost-effective approach.

A hint about the first simplification follows from the short time scales of the physical processes under consideration. Bykov *et al.* (2024) [32] found that it takes significantly less than  $10^5$  s for the complete expansion of the nebula and the accompanying acceleration of protons to PeV energies, provided that the expansion starts from zero in a stellar wind with a Gauss-range field. This is very short compared to the orbital period of known gamma-ray binaries with pulsars [33, 34]<sup>2</sup>. This is even shorter than the estimated periastron passage time during which one would expect efficient acceleration of PeV regime protons in the case of elongated orbits with periods more than a year like in PSR B1259-63 and PSR J2032+4127. Rapid inflation allows the nebula to easily adjust its flow structures to local stellar wind conditions. Moreover, according to [32], the strong magnetic field in the wind collision region becomes the main factor shaping its structure, making the magnetic force dominant over the Coriolis force induced by the orbital motion of the pulsar. With this in mind and taking into account the rapid acceleration of particles, one can consider only

<sup>2</sup> Interestingly, gamma-ray binaries with black holes that have very short periods have also smaller orbital separation distance and, therefore, stronger magnetic field in the colliding flow region, that, in principle, allows similar consideration

the *local structure* of the region of the colliding flows. This greatly simplifies the problem. There is little point in monitoring this region for most of the pulsar's orbit, where the field's influence on the structure is weak or the parameters of the wind collision zone do not facilitate multi-PeV particles acceleration.

In the considered objects, the region of direct wind collision can be very compact. According to [32], the nebula bubble can occupy a volume more than two orders of magnitude smaller than it would have inside the supernova remnant. If this bubble is small compared to the distance between the binary companions, the problem can be simplified even further (especially given the shortness of the dynamical and acceleration time scales). In the *local vicinity* of the bubble, the stellar wind flow can be considered uniform, with fixed directions of field and velocity. Another simplification follows from the fact that in a strongly magnetized stellar wind, the flow velocity tends to align with the magnetic field.

The above reasoning reduces a computationally efficient setup for studying the acceleration of PeV protons in gamma-ray binaries to the following. We consider a pulsar wind nebula inflating in a dense, uniform, strongly-magnetized flow with aligned magnetic field and velocity. The magnitudes of the field and velocities, as well as pressure and mass density, are prescribed by modern stellar wind models [e.g., 35, 36]. The consideration is local and includes the nebula itself and its immediate surroundings. Bykov *et al.* [32] noted that the acceleration of multi-PeV particles may not be sensitive to the symmetry of the system: only the size of the acceleration site and the spectrum of upscattering magnetic inhomogeneities in it play a decisive role. With this in mind, they performed planar (2D) modeling of gamma-ray binaries. Here we simulate and analyze the flows structure in 2D and 3D and discuss the validity of planar models.

### III. MODELING RESULTS

#### A. 2D and 3D nebulae developing in a strongly magnetized stellar wind

To compare the 2D and 3D structures of a nebula immersed in a highly magnetized stellar wind ( $sw$ ), we ran two corresponding sets of rMHD models and tested them for different values of  $B_{sw}$ . The models are listed in Table I, and Fig. 1 depicts the results. For any of the studied models, the nebula forms within a few hours. Its MHD structure, arising from interactions with the stellar wind, then evolves in a self-similar manner. The structure is shown in Fig. 1 using the  $B$  field maps. The maps are snapshots of a 2D nebula in its meridional cut (left column) and a 3D nebula in its meridional and equatorial cuts (middle and right columns, respectively). In each column, the maps are arranged to illustrate the effect of increasing the strength of the stellar wind field  $B_{sw}$ .

In the meridional cuts, the structure of magnetized

flows in 2D and 3D runs turns out to be very similar and can be briefly described as follows. The pulsar, sitting in the center of the bubble, emits cold relativistic pulsar wind (*blue region*). The wind then abruptly decelerates and heats up at the termination shock. The wind zone and shock both appear  $\infty$ -shaped because the wind is stronger near the nebula's equator than near its poles [37]. Not only the power but also the wind field is anisotropic: it reaches a maximum at mid-latitudes and drops sharply toward the poles and equator (e.g., [38]; see details in Appendix A). Because of the combination of these anisotropies, the wind flow approaching the shock is weakly magnetized at equatorial latitudes and strongly magnetized at higher latitudes, where the shock is closer to the pulsar. When crossing the inclined parts of the shock wave, the wind's radial streamlines are deflected and plasma magnetization increases – again, depending on latitude. A smooth change in the angle of deflection along the inclined (arch-shaped) parts of the shock allows the latter to collect strongly magnetized plasma into two narrow-channel streams (*shown in dark red*), tightly pressed against its front, and focus them toward the equator. There, the streams begin to mix and intertwine. Because they originate in hemispheres with different magnetic polarities, their mixing results in a turbulent, highly magnetized outflow. Its magnetic inhomogeneities can propagate outward with  $v/c \sim 0.5\text{--}0.85$ , depending on the model. To a distant observer, such outflow could result in the appearance of an X-ray torus (or double-torus), a synchrotron feature often seen in synchrotron images of subsonic or slightly supersonic pulsar wind nebulae (PWNe) [9, 39–44].

In many ways the picture described above resembles that seen in models of isolated pulsar wind nebulae. Examples include models of the subsonic Crab Nebula [45–52] and the slightly-supersonic Vela nebula [53]. However, there are a number of differences, which are listed below. (1) In gamma-ray binaries, the nebulae are much more compact, therefore they accumulate the magnetic energy much faster. Their magnetic fields are in the sub-Gauss range and can even reach  $\sim$  Gauss, while in isolated nebulae they barely exceed a few hundred micro-Gauss. (2) Another difference is that an X-ray torus may look tilted toward the equator of the nebula. The tilt of the torus can gradually disappear as the pulsar approaches apastron and recover again as it approaches periastron. (3) In gamma-binaries, the nebula bubble is surrounded by a dense magnetic cocoon that forms from the stellar wind material perturbed by the bubble's expansion. This cocoon is of paramount importance for accelerating very high-energy particles, and we will discuss it a little later. (4) The nebula can form relativistic clumps – unusually-fast magnetic inhomogeneities not observed (at least not yet) in models of isolated nebulae. These clumps can act as scattering centers, capable of providing particularly efficient acceleration of high-energy particles. (5) Finally, the nebular bubble can be significantly contracted across the field direction, as it described below.

Along the  $B_{sw}$  field direction the size of the bubble is determined by the balance of the ram pressure of the stellar wind and the pressure inside the nebula. Across this field, the bubble expansion is additionally limited by the tension of the magnetic field lines. The way in which the bubble proportions respond to increasing  $B_{sw}$  is illustrated by the successive rows in Fig. 1 in which this field is taken to be 0.5, 1, 2 and 3 G, from top to bottom. Comparing the maps in the left and middle columns, one can see that the 2D and 3D bubbles evolve in a similar way and have similar shapes, despite the strong differences in their pulsar and stellar wind parameters (see Table I). This is especially noticeable in the limit of a strong field of 2 to 3 G. The shape of the bubble is formed under the influence of two anisotropies: the latitudinal anisotropy of the pulsar wind power and the one caused by the misalignment of  $\mathbf{B}_{sw}$  and the pulsar's rotation axis (which is vertical in the plane of the maps). At lower fields – 0.5 and 1 G – the first factor predominates, and the bubble is more extended in the equatorial direction, around which the pulsar wind is more powerful. At stronger fields – 2 and 3 G – the magnetic tension of the  $\mathbf{B}_{sw}$  lines takes over, and the bubble stretches along their direction. The field strength at which this transition occurs can be estimated by equating the magnetic pressure  $B_{sw}^2/8\pi$  in the stellar wind to the momentum density flux at a distance  $r$  from the pulsar,  $\Phi = \dot{E}/4\pi r^2 u_{pwn}$ , carried by nebular ( $pwn$ ) flows expanding at a velocity  $u_{pwn}$ :

$$B_{sw} = \left( \frac{2\dot{E}}{u_{pwn} r^2} \right)^{1/2} \quad (1)$$

$$= 0.5 \dot{E}_{37}^{1/2} \left( \frac{u_{pwn}}{0.1c} \right)^{-1/2} \left( \frac{r}{10 \text{ AU}} \right)^{-1} \text{ G}.$$

The estimate suggests that in fields  $B_{sw} \sim 1$  G and above the nebula bubble will be noticeably elongated in the directions of the field, even if the wind power is as high as  $\dot{E} \sim 10^{37} \text{ erg s}^{-1}$ . This is indeed observed in Fig. 1, both in 2D and 3D runs. For a given  $B_{sw}$ , the ratio of the longitudinal to transverse size for 2D and 3D bubbles is similar: it is  $\simeq 0.5$  for 2 G and  $\simeq 0.3\text{--}0.35$  for 3 G.

At the same time, the equatorial size of 2D and 3D bubbles (on meridional cuts) remains practically unchanged, and therefore the size of the X-ray torus too, despite the fact that the bubble shrinks in the total volume. The torus is simply reshaped from axially symmetric to oval due to a slight flattening across the field when it is amplified by  $\sim 6$  times. In addition, the torus gradually acquires a tilt toward the nebula's equator (determined by the plane of the pulsar's rotational equator). This occurs because the strongly magnetized equatorial outflow, which creates the appearance of the torus to a distant observer, tends to be deflected in different directions from the equator on the leeward and windward sides of the nebula. In essence, this outflow gradually transforms from disk-shaped to S-shaped with increasing field strength in the stellar wind. The tilt of the torus can change gradually along the pulsar's orbit, reaching a minimum at

apastron and a maximum at periastron.

Although at kpc distances the modern X-ray telescopes cannot resolve X-ray tori smaller than 100 AU in size, their radio counterparts may, in principle, be resolvable by radio telescopes. The change in the tilt of the torus, assuming that the effect is observed, can be used to track the change in the  $B_{sw}$  strength along the pulsar's orbit. The effect can even help to constraint the strength itself, if other parameters affecting the torus appearance have already been constrained at the apastron (assuming that the field effects are negligible there). In sub-Gauss fields, the X-ray torus will be highlighted by synchrotron radiation from electrons with Lorentz factors of about  $10^6$ . Such electrons can, in principle, come directly with the pulsar wind, so their number can be few orders of magnitude greater than that of accelerated electrons with Lorentz factors above  $10^8$ , which are usually responsible for the soft X-ray radiation of an isolated pulsar's nebula.

Unlike the torus, the shock wave retreats as the field increases. This is most clearly seen in the right column in Fig. 1. This behavior is expected. The dynamic pressure of the stellar wind increases as  $\rho u_{sw}^2 + B_{sw}^2/8\pi$ , causing the bubble to decrease in volume. So the average magnetization of the plasma in the remaining volume goes up. This brings into play an effect well known in modeling nebulae of isolated pulsars: as the average magnetization in the nebula increases, the termination shock moves closer to the pulsar, and the polar jets<sup>3</sup> become more powerful [45, 46]. Our simulations indicate that the local MHD structure of the pulsar wind nebula depends more than moderately on the velocity and density of the stellar wind, as long as the latter is strongly magnetized.

Let us turn to the magnetic cocoon. The expanding bubble perturbs the stellar wind, which eventually leads to the creation of a shell of compressed stellar-wind matter around the nebula. This shell can be several times denser than the undisturbed wind. The field in the shell (being frozen into the plasma,  $B \propto \rho$ ) can also be several times stronger than the unperturbed  $B_{sw}$ , and fall into the Gauss-range even if  $B_{sw}$  is at sub-Gauss. In essence, the shell acts as a kind of magnetic cocoon capable of holding high energy particles within the accelerator – the wind collision region that encloses the nebula and the cocoon itself. The PeV particles may only be held there for a few hours, but that is still long enough for them to gain an energy above 10 PeV before leaving the region [32]. As  $B_{sw}$  increases, the bubble gives off more and more of its volume to the magnetic cocoon that forms around it. At the same time, the total volume of the region of wind collision changes little, at least in the 2D case (as can be seen in the left column in Fig. 1). In the 3D case the total volume seems to increase, but this is most likely

<sup>3</sup> In our models, jets – strongly collimated polar outflows – are not observed, since their formation requires the use of a much finer numerical grid than ours; see, e.g., [48], for more details.

a numerical effect. Due to their resource-intensive nature, our 3D runs were not as long as the 2D runs; they were stopped when we were convinced that the 3D nebula had reached the stage of self-similar evolution (Fig. 2); it seems that this was not enough time for the cocoon to fully form. So the effect is still to be checked. Finally, we note the presence of noticeable magnetic and density inhomogeneities in the cocoon. They are barely visible in Fig. 1 since its color palette is aimed at highlighting the MHD structures in the body of the nebula, not in the cocoon. Inhomogeneities form despite the fact that in our models of gamma-ray binaries the unperturbed wind of a massive companion is considered to be homogeneous, with a uniform magnetic field. The dynamics of these inhomogeneities is still to be studied, but their very presence may be important for the confinement and acceleration of high-energy particles.

As shown above, the 2D and 3D results have much in common. However, it is worth noting some of their differences. For the same gamma-ray binary parameters, the pressure inside the three-dimensional nebula is more uniform, and the MHD flows are less turbulent. These findings are consistent with the results of Porth *et al.* [48], pioneers in 3D modeling of isolated pulsar wind nebulae. They showed that the third degree of freedom destroys the artificially increased coherence of MHD flows in the presence of a purely toroidal field in the (axisymmetric) 2D nebula and softens their impact on the termination shock. Being more stable, the 3D shock in turn excites less energetic driven-scale turbulence in the downstream [47, 53]. Overall, a more uniform pressure in the nebula leads to a smoother shock wave profile; it also smooths out the outlines of the cocoon and nebula itself, making the cocoon’s irregularities less pronounced.

## B. Relativistic clumps

In their 2D models of gamma-ray binary systems, Bykov *et al.* [32] noted the appearance in the nebular outflows of “relativistic clumps” – especially fast-moving magnetic inhomogeneities with Lorentz factors  $\Gamma \gtrsim 3$  and sub-AU sizes. Such clumps are of great importance for Fermi-type particle acceleration to energies above PeV. Accelerating particles gain energy in head-on collisions with magnetic inhomogeneities in turbulent flows. In a single head-on collision, a particle can boost its energy by a factor of  $\Gamma^2$ , i.e., by the squared Lorentz factor of the encountered inhomogeneity. For the energy gain to be so significant, the inhomogeneity must be comparable in size to the particle’s gyroradius. The sub-AU scales of the relativistic clumps allow them to effectively upscatter pre-accelerated sub-PeV particles, since the latter have gyroradii  $\lesssim 1$  AU in the Gauss-range magnetic fields typical of nebulae in gamma-ray binaries. For the clumps, the factor  $\Gamma^2$  is almost an order of magnitude as large as that for the usual magnetic inhomogeneities.

Therefore, the clumps are much more efficient and can turn a sub-PeV particle into a PeV one in just a few successful scatterings.

The nature of the large-scale relativistic clumps remains to be elucidated. The clumps seem to form differently than the usual large-scale magnetic inhomogeneities. The latter arise in the form of magnetic eddies at the rims of the wind termination shock due to strong distortions of its working surface<sup>4</sup> [47, 48]. The shock wave then throws them into the nebula, where they quickly cascade and are advected outward by the turbulent equatorial flow. Their  $\Gamma$ -factors can be estimated from observations of the Crab Nebula and from rMHD simulations of nebulae in general. In Crab, the usual inhomogeneities are seen in radio, optical, and X-rays as fine, prominently bright arch-shaped synchrotron features (the so-called *wisps*). They originate at the wind termination shock and propagate outward with  $v/c \sim 0.5$ – $0.6$ , corresponding to  $\Gamma \sim 1.2$  [40]. Similar Lorentz factors are demonstrated by large-scale eddies in the equatorial flows in rMHD models<sup>5</sup> of Crab-like nebulae, objects with a single-torus morphology in X-rays. A characteristic feature of these objects is that flows of opposite magnetic polarities, arising in different hemispheres of the nebula, meet and mix right after the wind termination shock, thereby giving rise to a turbulent equatorial flow (details on the topic can be found in recent reviews [55–57]).

Meanwhile, the relativistic clumps appear to originate not at the shock, but at some distance from it, deep in the nebula. They certainly correlate with strong depressions that occur on either side of the wide, overcompressed, weakly-magnetized equatorial flow, where it temporally collapses or narrows greatly. Such equatorial flow is characteristic of another type of pulsar wind nebulae represented by Vela, an object with a double-torus X-ray morphology (Sect. III C). To form a double-torus, a pulsar must be in sub-sonic or slightly-supersonic motion relative to the external matter and have a wind with low average magnetization ( $\lesssim 0.002$ ; see [53, 58] for more details). Models *X1–X4* in Table I meet these conditions, so their flow pattern resembles that in the Vela-type nebulae. There, outflows of opposite polarity on either side of the overcompressed equatorial flow remain strongly-magnetized, quasi-laminar and ultra-relativistic, and do not mix up to distances of 2–3 shock radii. Their typical Lorentz factors can come to  $\Gamma \sim 1.5$ – $1.9$  (corresponding to  $v/c \sim 0.7$ – $0.85$ ) [53, 58]. The clumps seem to

<sup>4</sup> Note that modern relativistic MHD models of PWNe are built on a simplified prescription for the pulsar wind, in which the wind itself is uniform (in terms of density); see details in Appendix A.

<sup>5</sup> This estimate applies to flows that have already been thrown into the nebula from the arched vaults of the termination shock. Flows still running along these vaults are very narrow and quasi-laminar and therefore cannot upscatter a PeV-regime particle, no matter how high their  $\Gamma$  is (this  $\Gamma$  is estimated in [54]).

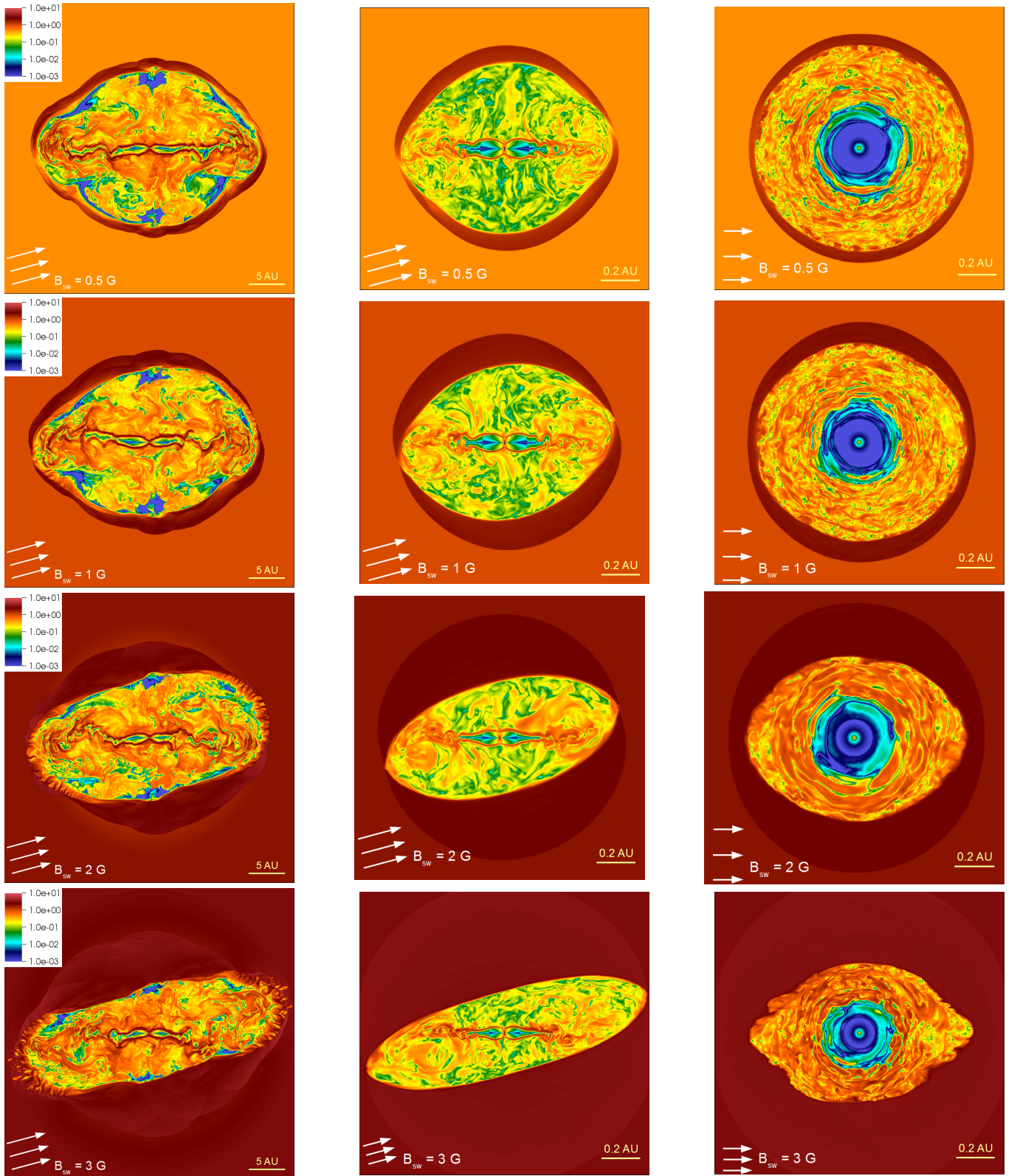


Figure 1. Wind collision region in 2D and 3D runs. Colors on the maps indicate the local magnetic field  $B$  [G]. Left column: 2D model (meridional cut). Middle and right columns: 3D model (meridional and equatorial cuts). The rows illustrate the effect of increasing the strength of the stellar wind field  $B_{sw}$ . From top to bottom:  $B_{sw} = 0.5, 1, 2$  and  $3$  Gauss.  $\vec{B}_{sw}$  is shown by white arrows and makes  $75^\circ$  with the pulsar's rotation axis (pointing upward in the 1st and 2nd columns and out-of-plane in the 3rd one). The color palette (the same in all panels) highlights the flow structures, not the maximum and minimum values of  $B$ . 2D and 3D setups corresponds to models  $A1$ – $A4$  and  $X1$ – $X4$  in Table I; we show their snapshots taken 15 and 2 hours after initiation, respectively.

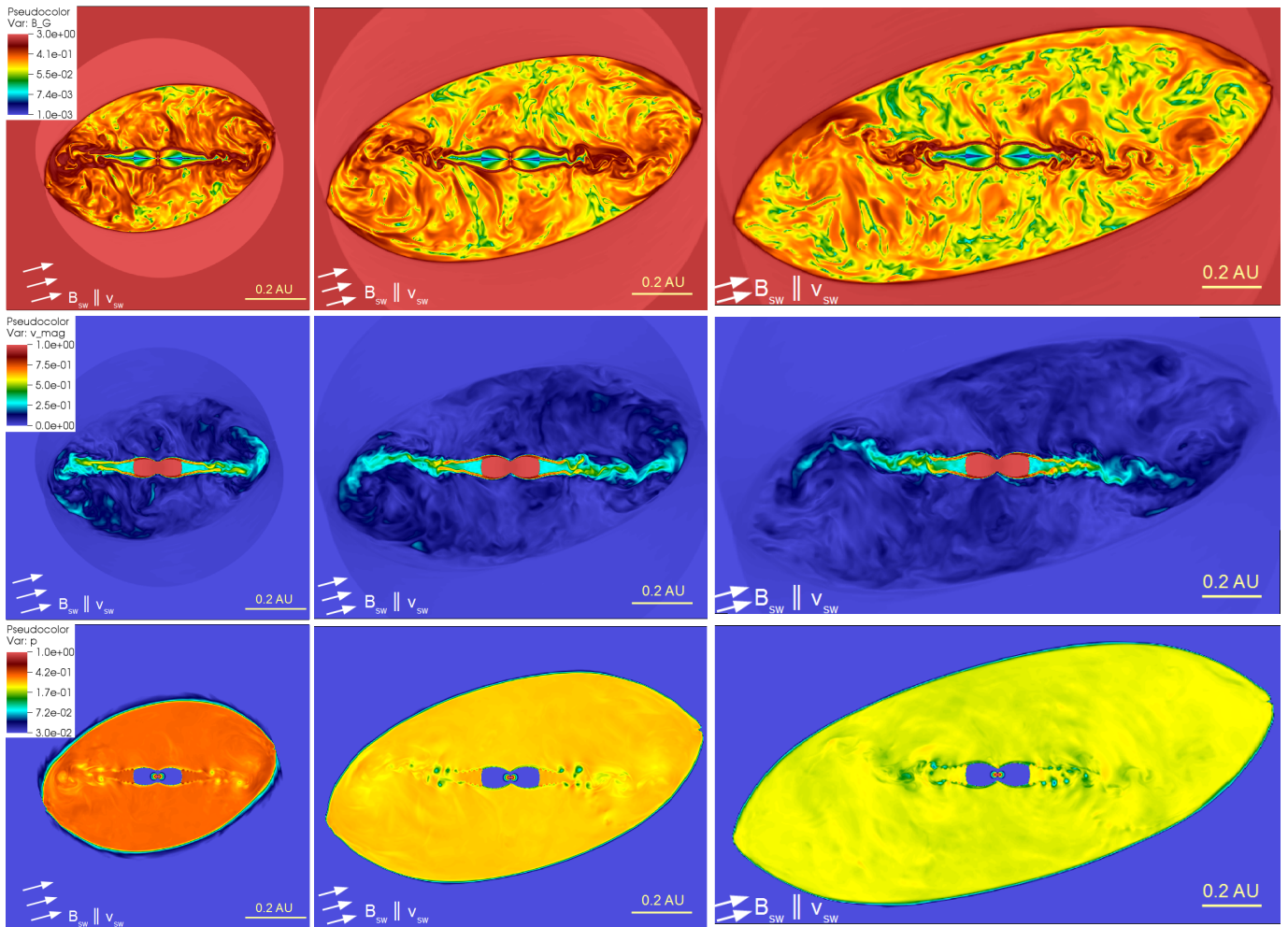


Figure 2. Time evolution of the pulsar wind nebula in gamma-ray binaries (3D case). The 3D nebula is shown in section by the plane defined by the pulsar’s rotation axis and the magnetic field vector of the stellar wind. The rows from top to bottom show maps of the magnetic field (in Gauss), velocity (in  $c$  units), and pressure (in cgs units). The maps describe the MHD flows (as they appear in the  $X\beta$  model from Table I in which  $B_{sw} = 2$  G). In each row, three consecutive maps are obtained at 0.8, 2, and 3 (model) hours after the onset of nebula inflation. The brightness scale of the color bar (universal for all maps in a particular row) is adjusted to highlight the flow patterns and does not reflect the maximum and minimum values of  $B$ ,  $v$  and  $p$ .

arise from the interplay of these strongly-magnetized relativistic flows with the overcompressed weakly-magnetized flow at the nebula’s equator.

The role of relativistic clumps in particle re-acceleration can be illustrated using a simple Monte-Carlo model (Appendix B). In it, a clump is modeled as a subregion embedded in the region of the relativistic wind, which in turn collides with the stellar wind. The embedded subregion is stationary, has a sub-AU size and high velocity with a certain  $\Gamma$ . A population of pre-accelerated particles is then injected in the system and allowed to interact with it. The result can be seen in Fig. 3 on the left panel. It shows several spectral energy distributions of the injected particles; namely, those that were:

- (1) just injected into the system;
- (2) accelerated in colliding flows alone;

(3/4/5) accelerated in colliding flows with the clump (with Lorentz factors  $\Gamma = 3/4.5/6$ , respectively). It can be seen that the acceleration in the colliding flows alone makes the spectral distribution much harder, with a single hump at sub-PeV energies. Embedding a clump with  $\Gamma \gtrsim 3$  in the colliding flows results in a double-humped spectrum with a second hump at energies well above PeV.

According to our 2D simulations, the clumps can arise in PWNe with very different parameters (see Fig. 4). The clumps with  $\Gamma \gtrsim 3$  can be more than 1 AU in size, i.e. larger, than the gyroradius of 10 PeV particles in a 1 G field. These clumps can persist in turbulent flows of the nebula for a few hours, which is more than enough time for re-acceleration to occur [32].

In agreement with the result of Porth *et al.* [48], in our 3D nebulae the termination shock is less dynamic

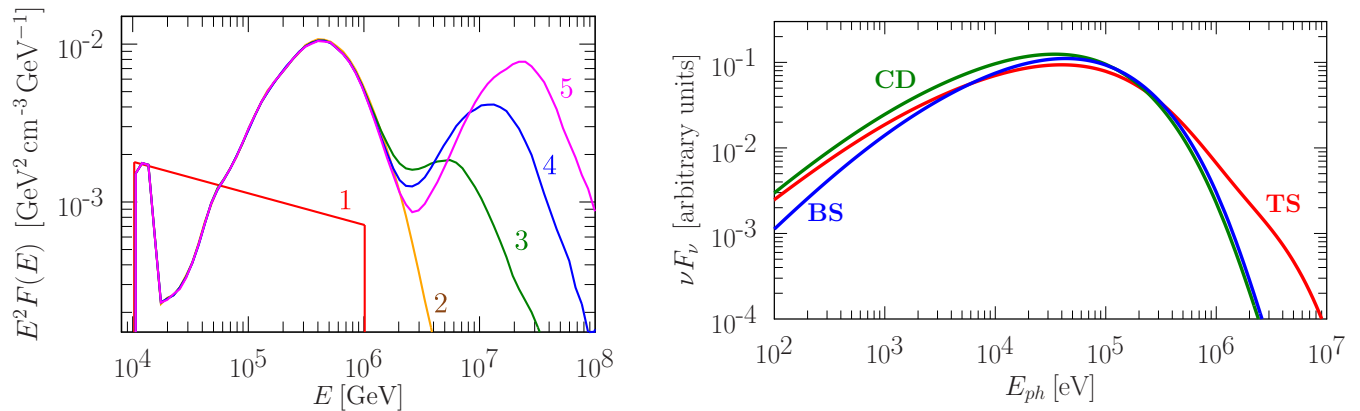


Figure 3. Left: Particle acceleration in the wind collision region of gamma-ray binaries (results of Monte-Carlo simulations). Several spectral energy distributions are shown in color: in red (1) – for the particles just injected in the system, in orange (2) – for those that were accelerated in the colliding flows alone, and in green, blue and magenta (3, 4, 5) – for those that were accelerated in the colliding flows with the relativistic clump. The last three spectra coinciding with the orange curve below 1 PeV =  $10^6$  GeV differ in the clump’s Lorentz factor, which is  $\Gamma = 3, 4.5$  and  $6$ , respectively. Right: simulated synchrotron spectra of the Vela-like pulsar wind nebula. Different colors refer to the synchrotron emissivity integrated over different lines of sight. Namely, over lines of sight coming close: to the termination shock (*TS*, in red), to the bow shock (*BS*, in blue), and to the contact discontinuity (*CD*, in green).

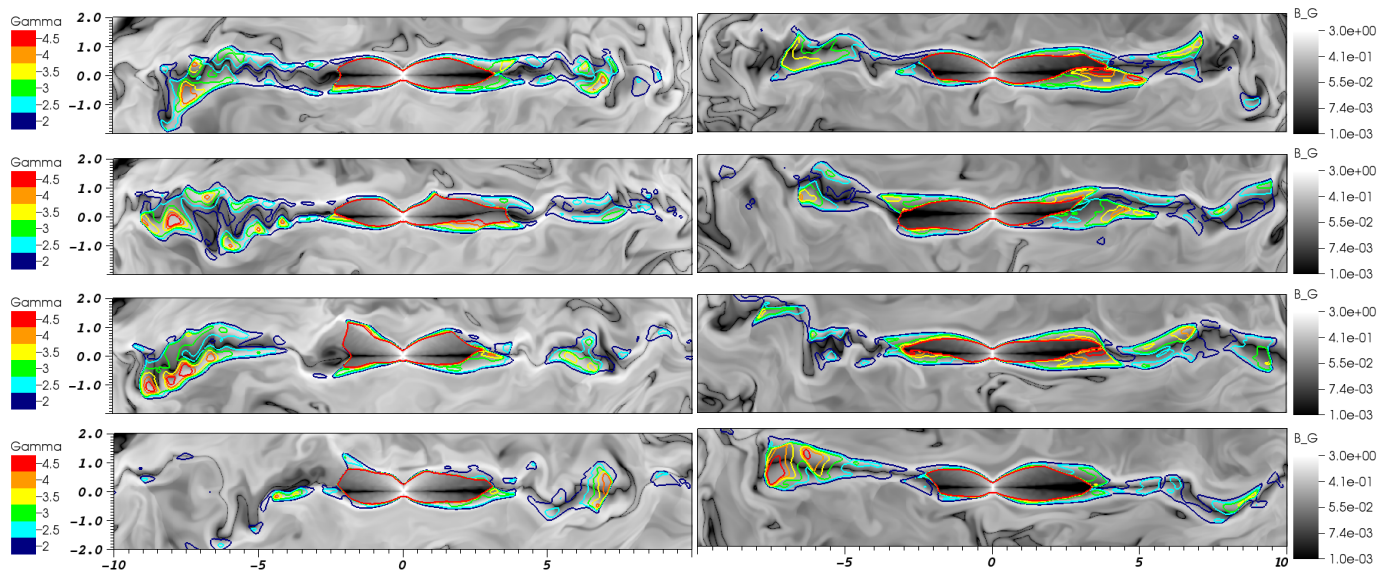


Figure 4. Relativistic clumps in pulsar wind nebulae (enlarged views of the equatorial region). Shown are 2D models *A5* and *A6* in Table I:  $\alpha = 45^\circ$ ,  $\sigma_0 = 0.3$  (left column) and  $\alpha = 80^\circ$ ,  $\sigma_0 = 3$  (right column). Contour plots of the Lorentz factor are superimposed onto gray-color maps of the magnetic field  $B$  [in G] provided to guide the eye. Each row corresponds to a certain point in time since the start of simulation:  $t = 11.1, 11.8, 12.5$  and  $13.2$  hours, from top to bottom. The gray-color bar is adjusted to highlight the structure of rMHD outflows and does not reflect the maximum and minimum values of  $B$ . Note that the contour  $\Gamma_{pw} = 4.5$ , that outlines the region of the unshocked pulsar wind, almost coincides with the position of the wind termination shock, due to the abrupt deceleration of the wind. The axes units are AU.

and magnetic turbulence is less intense. Despite this, we found that particularly fast-moving magnetic clumps still form in the nebula, although smaller in size and with lower  $\Gamma$ . This can be seen in Fig. 5, in the bottom two rows. In models with  $\alpha = 80^\circ$  the clumps have  $\Gamma \gtrsim 2$  and sizes of several percents of AU in the meridional plane (where the pulsar’s spin axis lies) and several tenths of

AU in the plane parallel to the equatorial plane of the nebula (Fig. 6). Whether this decrease in size and speed of the clump is a feature of 3D nebulae or a consequence of the insufficiently high resolution of 3D models remains to be seen. Our calculations indicate that the 3D clumps are larger, faster and more numerous the more strongly the pulsar wind is magnetized.

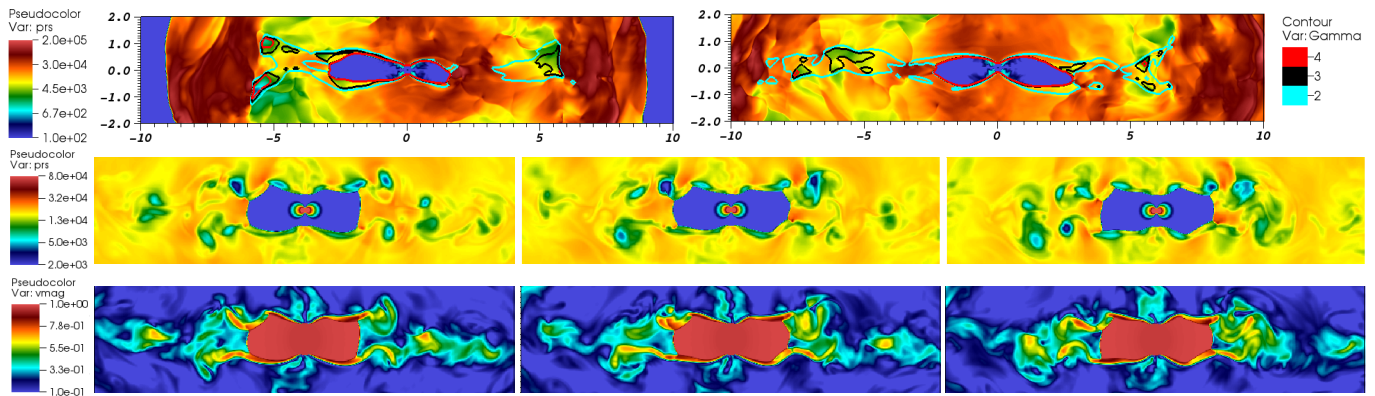


Figure 5. Relativistic clumps in pulsar wind nebulae (enlarged views of the equatorial region). Results of 2D/3D rMHD simulations of the colliding winds region in gamma-ray binaries. Top row (2D case): Colored pressure maps with superimposed contour plots of Lorentz factors of MHD-structures with  $\Gamma > 2$ . The maps show the nebula 7.6 and 9.7 (model) hours after the onset of its inflation. The calculation is based on the model *A5* from Table I ( $\alpha = 45^\circ$  and  $\sigma_0 = 0.3$ ). The axes units are AU. Middle and bottom rows (3D case): Correlation of depressions and clumps with a high Lorentz factor. Shown are colored maps of pressure (middle row) and flow velocity (in units of  $c$ ; bottom row). Successive maps in the rows are obtained at time points spaced  $\sim 100$  seconds apart, starting at 1.3 (model) hours after the onset of nebula inflation. The calculation is based on the model *X6* in Table I ( $\alpha = 60^\circ$ ,  $\sigma_0 = 0.1$ ). Pressure colorbars are in units of  $p_0 = 9 \cdot 10^{-6}$  dyn $\cdot$ cm $^{-2}$ . The brightness scales of the colorbars are adjusted to highlight the structure of flows and do not reflect the maximum and minimum values of the quantities.

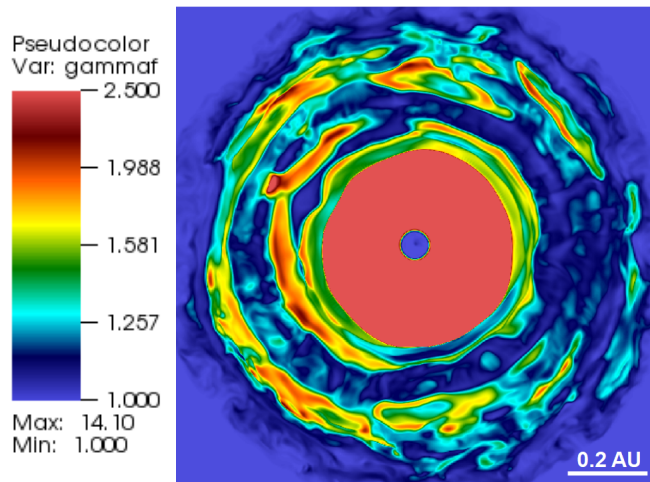


Figure 6. Color map of the Lorentz-factor  $\Gamma$  of rMHD flows (3D model nebula *X5* from Table I). Shown is a cross-section of the nebula by a plane parallel to its equatorial plane and offset from it by 0.058 AU. The brightness scale of the color bar is adjusted to highlight the structure of rMHD flows and does not reflect the maximum and minimum values of  $\Gamma$ .

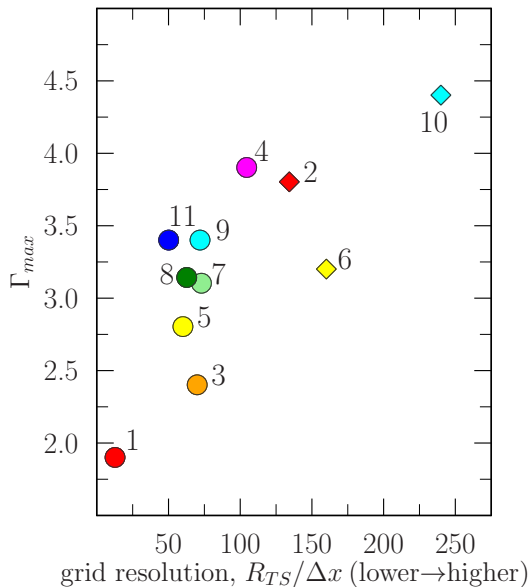
Relativistic clumps appear over a wide range of grid resolutions and over a large region of parameter space. As expected, their sizes and Lorentz factors depend on resolution of the numerical grid<sup>6</sup>. This is illustrated in

<sup>6</sup> they also depend on the convergence of the numerical scheme on which the numerical code is based; examples in the field of PWNe modeling can be found, e.g., in Porth *et al.* [48]

Fig. 7 for a number of 2D setups. This is a standard situation within the framework of an ideal rMHD approach, in which artificial numerical viscosity (determined by grid resolution) substitutes the real plasma viscosity.

### C. Astrospheres of isolated pulsars: the case of Crab and Vela

Like nebulae in gamma-ray binaries, nebulae of isolated pulsars can also be subject to a strong external flow. Examples include the Crab and Vela X-ray nebulae, not to mention highly supersonic objects. Crab appears to be influenced by the ejecta flow caused by the asymmetric expansion of the supernova remnant. This strong flow moves in almost the same direction as the pulsar, but faster than it. Taking this fact into consideration is important for interpreting synchrotron features observed in the nebula – its asymmetric jets, and the “inner ring” associated with the termination shock [52]. In turn, Vela encounters a fast counter-flow that appears slightly supersonic in the pulsar’s reference frame; it was initiated by a reverse shock of a supernova that swept over the nebula some time ago [59]. Taking this counter-flow into account is necessary for interpreting virtually all synchrotron features of Vela’s X-ray morphology, from its enigmatic double-torus to its complexly structured asymmetric jets [53, 58, 60]. The counter-flow is also the most natural cause of the quasi-periodic dynamics of these features, including the observed reverberations of the double-torus and even its precession [61], signs of which were detected by the Chandra X-ray telescope [62, 63].



Model	$\alpha$	$\sigma_0$	$n_{sw}, \text{cm}^{-3}$	$B_{sw}, \text{G}$	$\psi, ^\circ$
1	$45^\circ$	0.03	300	0.1	90
2	$45^\circ$	0.03	300	0.1	90
3	$45^\circ$	0.1	300	0.1	90
4	$45^\circ$	1	300	0.1	90
5	$85^\circ$	0.03	300	0.1	90
6	$85^\circ$	0.03	300	0.1	90
7	$45^\circ$	0.03	3000	0.4	45
8	$45^\circ$	0.03	30000	0.4	45
9	$45^\circ$	0.03	30000	0.1	45
10	$45^\circ$	0.03	30000	0.1	45
11	$45^\circ$	10	30000	0.4	45

Figure 7. Maximum Lorentz factor of relativistic clumps as a function of numerical grid resolution, for different 2D rMHD setups (shown in the table). The resolution is parameterized by the number of grid’s nodes within the equatorial radius  $R_{TS}$  of the termination shock. Symbols of the same color correspond to models with the same setup, which differ only in grid resolution.

In the presence of a strong external flow, the nebular flow pattern may become more regular, and the wind termination shock more stable<sup>7</sup>. Earlier 2.5D rMHD simulations<sup>8</sup> [58] showed that the shock stability is an essential condition for the formation of a double-torus in nebulae fed by a pulsar with a high magnetic inclination and a weakly magnetized wind. Such nebulae are distinguished by the presence of a barely magnetized and overcompressed equatorial flow with pulsations – oblique and normal shocks – by means of which the flow equalizes its pressure with neighboring regions of the nebula. Our current simulations confirm that the equatorial flow

<sup>7</sup> this refers to the stability of the shock geometry, not the shock transition itself

<sup>8</sup> 2.5D refers to an axisymmetric numerical grid without equatorial symmetry

exhibits pulsations in the 3D case as well. They can be seen in the pressure maps in Fig. 2, describing the full-dimensional  $X3$  model (in Table I). This model, like the Vela model in [58], is characterized by a high inclination, weakly magnetized wind, and expansion strongly constrained by the external flow.

Finally, the strong external flow appears to be necessary for spectral modeling of Vela. Its hard X-ray photon indices can be understood in a model in which a pulsar wind collides with a slightly supersonic flow. This was shown in Monte Carlo simulations of particle acceleration in collision of such flows [64]. Interestingly, this model predicts a significant flux of synchrotron radiation from Vela in the MeV range. This is shown in the right panel on Fig. 3 which depicts the simulated spatially-resolved synchrotron spectra of Vela. They were obtained by integrating, along certain lines of sight, the synthetic synchrotron emissivity calculated in each cell of a three-dimensional grid covering the volume of the model nebula. The particle spectrum in each cell was simulated using Monte Carlo approach. The color of the synchrotron spectra in Fig. 3 indicates where the corresponding line of sight intersects the nebula: *red* – near its wind termination shock; *blue* – near its bow shock, formed by the interaction with the external flow; *green* – near the contact discontinuity between these two shocks. Note that the model predicts the MeV flux only a few times lower than the X-ray flux detected by Chandra.

The potentially detectable MeV flux is likely a common feature of astrospheres of pulsars – both isolated and in gamma-ray binaries – that are energetic enough to produce charged particles in the PeV-range. In Vela and Crab, the pulsars can accelerate sub-PeV particles due to their high spin-down luminosity —  $\dot{E} \sim 7 \times 10^{36}$  and  $5 \times 10^{38} \text{ erg s}^{-1}$  (almost completely converted into the energy of the pulsar wind), while pulsars in gamma-ray binaries — even with a lower spin-down luminosity — due to the strong magnetic field in the powerful stellar wind of their massive companion.

#### IV. CONCLUSIONS

In this paper, we considered modeling the structure of the wind collision region in gamma-ray binaries, where the relativistic outflow of a compact object collides with the strongly magnetized wind of an early-type massive companion star. The collision wind region can have a few a.u. scale and can’t be resolved in observations. To demonstrate the ability of colliding winds, we simulated the interaction of a strongly magnetized stellar wind with a relativistic pulsar wind, based on well-established models of isolated pulsar wind nebulae. The models setups were thoroughly tested using a wealth of high-resolution radio, optical, and X-ray images of extended isolated galactic nebulae (such as Crab and Vela) and their spatially resolved spectra. We believe that the process of accelerating ultra high energy particles by intermittent

relativistic turbulence in the collision region can work reasonably well in gamma-ray binaries containing black holes accreting at critical rates and producing powerful outflows.

The present study shows that two-dimensional (2D) and full-dimensional (3D) models produce very similar results when simulating relativistic MHD flows in gamma-ray binaries. This indicates that the planar 2D models as those considered by Bykov *et al.* [32] can be safely used to study gamma-ray binaries as potential Pevatrons, particle (proton) accelerators up to petaelectronvolt (PeV) energies. Previously, the qualitative similarity of 2D and 3D models were demonstrated by Bosch-Ramon *et al.* [26] within the framework of the relativistic hydrodynamic approach when studying the influence of orbital motion on the pattern of flows in gamma-ray binaries. At contrast to the HD approach, our simulations take into account the strong Gauss-range magnetic field, that may be present in the wind of a massive companion (an early-type star) at distances up to a few astronomical units from it. The orbital motion of a compact companion (a pulsar) may bring it to these distances, especially in short-period or highly eccentric gamma-ray binaries.

The strong stellar-wind field causes the nebula to appear elongated, squeezing it across the field. Similar elongated shapes can be acquired by plerionic-type supernova remnants in magnetized circumstellar environments, as shown by non-relativistic 2D MHD simulations of Meyer *et al.* [65]. At the same time, the equatorial size of the nebula remains virtually unchanged even in a field  $\sim 3$  G. The same applies to the size of the X-ray torus, since this synchrotron feature of the nebula is formed precisely by its equatorial flows. The torus can acquire a tilt toward the nebula's equatorial plane if the magnetic field of the stellar wind makes an angle with the rotation axis of the pulsar. The tilt can change gradually along the pulsar's orbit, reaching a minimum at apastron and a maximum at periastron.

A strong field is of paramount importance for accelerating particles, as it can ensure their confinement in the accelerator, the region where the pulsar wind and the stellar wind collide. This compact region encompasses the pulsar wind nebula and the dense magnetic cocoon that formed around it from the stellar wind material. We found that the field in the 2D and 3D cocoons can reach a few Gauss, even though it is sub-Gaussian in the unperturbed stellar wind. The cocoon is capable of confining PeV particles within the nebula for only a few hours, but this is enough for them to gain energies above 10 PeV before escaping the wind collision region. Thus, the Pevatron accelerator in gamma-ray binaries can be switched on for a quite short interval of time during each orbital period. This does not prevent it from accelerating protons well above the limit determined by the magnetospheric potential of the pulsar. (In principle, the acceleration can be continued if PeV protons emerging from the accelerator can be upscattered by magnetic inhomogeneities in the stellar wind).

Inside the nebula, the rapid acceleration can be provided by fast flows capable of producing highly-magnetized, relativistic clumps with scales comparable to or larger than the gyroradii of PeV protons. Due to their high Lorentz factors, the clumps can increase the energy of sub-PeV particles above PeV in just a few successful scatterings. We show that such clumps can arise in 2D and 3D nebulae, although they seem to form differently from usual magnetic inhomogeneities in the flows. The maximum Lorentz factors of the clumps depend on the numerical resolution of the model, which is typical situation in an ideal magnetohydrodynamics, in which the real viscosity is substituted by a numerical one determined by the minimum spatial (and temporal) scales resolved by the numerical grid. In our higher resolution 2D models, the Lorentz factor can reach 4.5. In computationally expensive 3D models with fewer mesh nodes per nebula volume, the factors are somewhat lower. It remains to be seen whether this is due to their lower resolution or to a smoother pattern of flows. Higher resolution simulations are required for this study. Although direct numerical simulations in [32] clearly showed the ability of gamma-ray binary models to accelerate multi-PeV protons, the limited spatial resolution of these models prevented us from obtaining proton spectra over the wide energy range necessary for interpreting the observations. Therefore, we simulated these spectra using test-particle Monte Carlo simulations, in which proton scattering rates in intermitten relativistic flows were parameterized over a wide energy range. The spectra are shown in the left panel of Fig. 3. Recent kinetic particle-in-cell simulations of particle acceleration by relativistic turbulence [66, 67] demonstrated that the mechanism is promising indeed for explaining the origin of the highest-energy particles.

In the model presented in this paper, we considered a powerful pulsar wind as the source of the relativistic outflow. In fact, many important features of the model hold for gamma-ray binaries where the compact companion is an accreting black hole. The powerful galactic microquasar Cygnus X-3 is a high-mass X-ray binary (HMXRB) with a period  $\sim 4.8$  hours; its compact object – either a black hole or a neutron star – accretes matter from a massive Wolf-Rayet companion star. Cyg X-3 produces, apart from X-ray emission, jet-driven radio flares. The LHAASO observatory detected time-modulated ultra-high-energy gamma-ray emission from this source, with energies up to a few PeV [68]. If the modulated PeV photon radiation is produced by the photomeson process [68], it would require protons accelerated well above ten PeV. The proton spectra presented in Fig. 3 (left panel), obtained from Monte Carlo simulations, demonstrate that a relativistic outflow colliding with the highly magnetized wind of a massive star can accelerate particles to multi-PeV energies. The resulting specific two-peak spectra may be useful for interpreting LHAASO data.

## ACKNOWLEDGMENTS

We acknowledge Georgy Ponomaryov for his contribution to our numerical studies of PWNe and gamma-ray binaries. Monte Carlo simulations by A.E.P. were supported by the Foundation for the Advancement of Theoretical Physics and Mathematics “BASIS”. Data analysis by K.P.L. was supported by the baseline project FFUG-2024-0002 at the Ioffe Institute. Some of the modeling was performed at the “Tornado” subsystem of the St. Petersburg Polytechnic University Supercomputing Center.

### Appendix A: rMHD modeling setups

Our rMHD simulations of gamma-ray binaries are based on Relativistic MHD Module of the code PLUTO [69]. In this study, we assume that the binary system harbors a pulsar orbiting a massive early-type star (here, a Be star). We examine the local structure of the region where the pulsar wind and the stellar winds collide. This region encompasses the pulsar wind nebula and the dense cocoon that forms around it from the stellar wind material. The stellar wind is initialized as a homogeneous, strongly magnetized flow with co-directional magnetic field and velocity, following the arguments in Sect. II. The wind’s parameters are given in Table I; they are chosen to illustrate the variety of conditions that the pulsar might encounter where its orbit takes it close to the Be star. Our simulations indicate that the local MHD structure of the pulsar wind nebula depends more than moderately on the velocity and density of the stellar wind, as long as the latter is strongly magnetized.

To inflate the nebula, we apply a simplified model of the pulsar wind that is widely used in modern rMHD simulations of isolated nebulae [e.g., 46, 48, 50, 51, 53], in the formulation given in [51]. In this model, the wind is cold and its energy flux density is latitudinally dependent, with a maximum at the plane of the rotational equator of the pulsar (this plane determines the equatorial plane of the nebula):

$$f_{tot}(r, \theta) = \frac{\dot{E}}{L_0} \frac{1}{r^2} \cdot (\sin^2 \theta + \varepsilon). \quad (\text{A1})$$

Here  $r$  is a distance from the pulsar,  $\theta$  – colatitude,  $L_0 = 4\pi(2/3 + \varepsilon)$  – normalization constant,  $\varepsilon = 0.02$  prevents the flux from vanishing at the poles. The energy flux is divided into magnetic and kinetic components,  $f_{tot} = f_m + f_k$ , the ratio of which is determined by the magnetization  $\sigma = f_m/f_k$  of the cold pulsar wind:

$$\begin{aligned} f_m(r, \theta) &= \frac{\sigma(\theta) \cdot f_{tot}(r, \theta)}{1 + \sigma(\theta)}; \\ f_k(r, \theta) &= \frac{f_{tot}(r, \theta)}{1 + \sigma(\theta)}; \\ \sigma(\theta) &= \frac{\tilde{\sigma}(\theta) \cdot \chi_\alpha(\theta)}{1 + \tilde{\sigma}(\theta) \cdot (1 - \chi_\alpha(\theta))} \end{aligned} \quad (\text{A2})$$

Magnetic field of the wind is purely toroidal and frozen into the plasma. The wind magnetization is latitudinally dependent: it almost vanishes near the rotational equator and toward the poles, and has a maximum at the middle latitudes. These features are accounted with the functions  $\tilde{\sigma}$  and  $\chi$ :

$$\begin{aligned} \tilde{\sigma}(\theta) &= \sigma_0 \cdot \min \left\{ 1, \frac{\theta^2}{\theta_0^2}, \frac{(\pi - \theta)^2}{\theta_0^2} \right\}; \\ \chi_\alpha(\theta) &= \begin{cases} (2\phi_\alpha(\theta)/\pi - 1)^2 & \text{if } |\pi/2 - \theta| < \alpha \\ 1 & \text{otherwise} \end{cases} \end{aligned} \quad (\text{A3})$$

with  $\phi_\alpha(\theta) = \arccos(-\cot(\theta)\cot(\alpha))$  and a typical value of  $\theta_0 = 10^\circ$ . Here  $\sigma_0$  is the initial magnetization, and the function  $\tilde{\sigma}$  describes its decrease toward the poles due to the azimuthal nature of the field ( $B \equiv B_\varphi \propto \sin\theta$ ). The function  $\chi_\alpha$  accounts for the fact that the wind magnetic field alternates at the equatorial latitudes within the angular sector  $\pi/2 \pm \alpha$ . As is known, the field of the pulsar changes sign at the pulsar’s magnetic equator. The latter usually makes a certain angle  $\alpha$  (called *magnetic inclination*) to the rotational equator of the pulsar. As the pulsar rotates, the wind magnetic field changes sign at the equatorial latitudes every half-period of rotation and hence the wind becomes striped. It carries the stripes of plasma of alternating magnetic polarity which fill the angular sector  $\pi/2 \pm \alpha$ . Either on their way to the wind termination shock, or due to their compression right at the shock, the stripes can annihilate [70–72], so the magnetic field in the equatorial sector  $\pi/2 \pm \alpha$  dissipates almost completely. For the pulsar wind’s density, magnetic field and velocity we have:

$$\begin{aligned} \rho_{pw}(r, \theta) &= f_k(r, \theta)/\Gamma_{pw}^2 c^3, \\ B_{pw}(r, \theta) &= \pm \sqrt{4\pi f_m(r, \theta)/c}, \\ u_{pw}/c &= \sqrt{1 - \Gamma_{pw}^{-2}}. \end{aligned} \quad (\text{A4})$$

The wind is radially directed and has a Lorentz-factor  $\Gamma_{pw} \gg 1$ . To maintain numerical stability,  $\Gamma_{pw} = 10$  is usually assumed, although this choice does not affect the calculation results as far as  $\Gamma_{pw} \gg 1$  (see [51] for details). Our numerical 2D/3D grids are Cartesian, with the y-axis aligned with the pulsar’s rotation and no z-axis in 2D space. The coordinates of the Cartesian and spherical systems are related as  $r = (x^2 + y^2 + z^2)^{1/2}$  and  $\theta = \arccos(y/r)$ .

### Appendix B: Simplified anisotropic Monte-Carlo model

To simulate particle acceleration in the wind collision zone of a gamma-ray binary – accounting for efficient particle scattering by turbulence with a wide range of spatial scales – we developed a massively parallelized numerical code based on the Monte Carlo approach. The code is

run	$B_{sw}$	$\psi, ^\circ$	$n_{sw}$	$p_{sw}$	$\dot{E}$	$\alpha, ^\circ$	$\sigma_0$	$\Gamma_{pw}$	box, $\text{au}^2/\text{au}^3$	core, $\text{au}^2/\text{au}^3$	$r_{in}, \text{au}$	$N_x$	$N_y; N_z$	$\Delta, \text{au}$
A1	0.5	75	$3 \times 10^4$	$10^{-7}$	$10^{37}$	45	3	100	$40 \times 40$	$40 \times 40$	0.15	1600	1600	0.025
A2	1	75	$3 \times 10^4$	$10^{-7}$	$10^{37}$	45	3	100	$40 \times 40$	$40 \times 40$	0.15	1600	1600	0.025
A3	2	75	$3 \times 10^4$	$10^{-7}$	$10^{37}$	45	3	100	$40 \times 40$	$40 \times 40$	0.15	1600	1600	0.025
A4	3	75	$3 \times 10^4$	$10^{-7}$	$10^{37}$	45	3	100	$40 \times 40$	$40 \times 40$	0.15	1600	1600	0.025
A5	3	45	$3 \times 10^4$	$10^{-7}$	$10^{37}$	45	0.3	100	$40 \times 40$	$40 \times 40$	0.15	1600	1600	0.025
A6	3	45	$3 \times 10^4$	$10^{-7}$	$10^{37}$	80	3	100	$40 \times 40$	$40 \times 40$	0.15	1600	1600	0.025
X1	0.5	75	$2 \times 10^5$	$10^{-4}$	$10^{35}$	80	0.3	4	$2 \times 1.46 \times 1.46$	$0.6 \times 0.6 \times 0.6$	0.02	340+600+340	252+600+252	0.001
X2	1	75	$2 \times 10^5$	$10^{-4}$	$10^{35}$	80	0.3	4	$2 \times 1.46 \times 1.46$	$0.6 \times 0.6 \times 0.6$	0.02	340+600+340	252+600+252	0.001
X3	2	75	$2 \times 10^5$	$10^{-4}$	$10^{35}$	80	0.3	4	$2 \times 1.46 \times 1.46$	$0.6 \times 0.6 \times 0.6$	0.02	340+600+340	252+600+252	0.001
X4	3	75	$2 \times 10^5$	$10^{-4}$	$10^{35}$	80	0.3	4	$2 \times 1.46 \times 1.46$	$0.6 \times 0.6 \times 0.6$	0.02	340+600+340	252+600+252	0.001
X5	0.5	45	$2 \times 10^6$	$10^{-3}$	$10^{37}$	80	0.3	4	$3 \times 3 \times 3$	$0.6 \times 0.6 \times 0.6$	0.027	363+451+363	363+451+363	0.0013
X6	0.5	75	$2 \times 10^5$	$2 \times 10^{-4}$	$10^{35}$	60	0.1	4	$2 \times 2 \times 2$	$0.6 \times 0.6 \times 0.6$	0.03	240+400+240	240+400+240	0.0015

Table I. Nebula models parameters. For the stellar wind ( $sw$ ):  $B_{sw}$  is the magnetic field in Gauss;  $\psi$  is the angle between  $B_{sw}$  and pulsar’s spin axis;  $n_{sw}$  and  $p_{sw}$  are the number density and pressure, in cgs units. In all setups, the stellar wind velocity is taken to be  $300 \text{ km s}^{-1}$ , as seen in the pulsar frame of reference [see, e.g. 35]. For the pulsar wind ( $pw$ ):  $\Gamma_{pw}$  and  $\sigma_0$  – the Lorentz-factor and initial magnetization;  $\dot{E}$  – the total power (the pulsar’s spin-down luminosity, in  $\text{erg s}^{-1}$ ); and  $\alpha$  – the angle between the rotational and magnetic axes of the pulsar. For the modeling domain: the “box” is its full spatial dimension, and the “core” is its central region ( $x_1 < x < x_2$ ,  $y_1 < y < y_2$ ,  $z_1 < z < z_2$ ) with a uniform grid of resolution  $\Delta$  and with a small area of radius  $r_{in}$  in the center, from which the pulsar wind is continuously injected.  $N_x, N_y, N_z$  are the total numbers of the grid nodes in the “box” in the  $x, y, z$  directions, respectively. In 2D setups the  $z$  axis is absent, while in 3D setups it has the same subdivision as the  $y$ -axis ( $N_y = N_z$ ). In 2D models  $A1$ – $A6$ , the entire grid is uniform (“core” $\equiv$ “box”), and  $N_x = N_y$ . In 3D models  $X1$ – $X6$ , the grid is patchy; its  $x$ -axis is subdivided as follows: its step increases logarithmically with distance below  $x_1$  and above  $x_2$ , and is uniform in the “core” between  $x_1$  and  $x_2$ ; the number of nodes in each interval of  $x$  is represented by the corresponding term in the sum in the  $N_x$  column. The same subdivision is applied to the  $y$  and  $z$  axes.

three-dimensional and takes into account the propagation of charged particles in a turbulent magnetic field with a strong regular component. Based on the simplified model of flow structure, it allows us to study the acceleration in the collision zone between a strongly magnetized stellar wind and a relativistic outflow –produced either by a pulsar (as in the present study) or by a black hole. The description below assumes a gamma-ray binary with a pulsar.

The computation domain is a cylinder with radius  $R_{box}$  and length  $l_{box} = 2R_{box}$  and a uniform magnetic field  $B_{box}$  parallel to the cylinder’s axis. Two colliding winds – pulsar and stellar – are modeled as two magnetized uniform flows, each of which occupies half of the cylinder. The winds’ velocities –  $\mathbf{u}_{pw}$  and  $\mathbf{u}_{sw}$  – are counter-directed and parallel to the cylinder’s axis. The contact discontinuity (CD) between the winds is represented by a narrow buffer region with zero flow velocity. A small cylindrical subregion emdedded in the region of the pulsar wind models the relativistic clump with  $\Gamma > 2$ . The simulation parameters reproduce the conditions in gamma-ray binaries:  $R_{box} \approx 3 \text{ AU}$ ,  $B_{box} = 0.1 \text{ G}$ ,  $u_{pw} = 0.57 c$  and  $u_{sw} = 800 \text{ km s}^{-1}$ . The clump has a size of  $0.6 \times 1.2 \text{ AU}$  and a flow velocity with a high Lorentz factor  $\Gamma$ . We considered the cases with  $\Gamma = 3, 4.5$  and  $6$ . The result of the Monte Carlo simulation is shown in Fig. 3, on the left panel.

The simulation of acceleration begins by injecting a population of nonthermal particles into the CD region. The injected population is assumed to be pre-accelerated (e.g., on the wind termination shock, TS), having an initial spectrum  $f_{TS}(E) \propto E^{-2.2}$ . The particles then move along their (helical) trajectories prescribed by Newtonian

laws for a certain free-flight time  $t_{mfp}$ . After that, each particle is scattered isotropically (in the rest frame of a local background flow), and moves again for time  $t_{mfp}$ , and so on, until it leaves the computational domain through its border with the free escape boundary conditions. The free-flight time  $t_{mfp}$  is determined by the mean free path  $\lambda_{mfp} = c \cdot t_{mfp} = \eta R_g$ , where  $R_g$  is the particle gyro-radius, with  $\eta = 6$  in the pulsar wind’s and the stellar wind’s regions and  $\eta = 12$  in the CD region.

## REFERENCES

- [1] V. V. Sobolev, *Moving Envelopes of Stars*, Harvard University Press (1960).
- [2] V. B. Baranov and K. V. Krasnobaev, *Hydrodynamic theory of a cosmic plasma*, Moscow Nauka (1977).
- [3] H. J. G. L. M. Lamers and J. P. Cassinelli, *Introduction to Stellar Winds* (1999).
- [4] A. ud-Doula, S. P. Owocki, C. Russell, M. Gagné, and S. Daley-Yates, 3D MHD models of the centrifugal magnetosphere from a massive star with an oblique dipole field, *MNRAS* **520**, 3947 (2023), arXiv:2301.11858 [astro-ph.SR].
- [5] E. N. Parker, *Interplanetary dynamical processes*, New York, Interscience Publishers (1963).
- [6] V. B. Baranov, K. V. Krasnobaev, and A. G. Kulikovskii, A Model of the Interaction of the Solar Wind with the Interstellar Medium, *Soviet Physics Doklady* **15**, 791 (1971).
- [7] J. D. Richardson, A. Bykov, F. Effenberger, K. Scherer, R. von Steiger, V. J. Sterken, and G. P. Zank, *The Heliosphere in the Local Interstellar Medium: Into the Unknown*, Springer (2023).
- [8] E. A. Godenko and V. V. Izmodenov, Dynamical

- charging of interstellar dust particles in the heliosphere, *Advances in Space Research* **72**, 5142 (2023), arXiv:2311.00505 [astro-ph.SR].
- [9] J. J. Hester, The Crab Nebula : an astrophysical chimera., *ARA&A* **46**, 127 (2008).
- [10] K. Fang, X.-J. Bi, and P.-F. Yin, Reanalysis of the Pulsar Scenario to Explain the Cosmic Positron Excess Considering the Recent Developments, *ApJ* **884**, 124 (2019), arXiv:1906.08542 [astro-ph.HE].
- [11] J. Arons, Pulsar Wind Nebulae as Cosmic Pevatrons: A Current Sheet's Tale, *Space Sci. Rev.* **173**, 341 (2012), arXiv:1208.5787 [astro-ph.HE].
- [12] G. Dubus, Gamma-ray binaries: pulsars in disguise?, *A&A* **456**, 801 (2006), arXiv:astro-ph/0605287 [astro-ph].
- [13] A. Neronov and M. Chernyakova, Radio-to-TeV  $\gamma$ -ray emission from PSR B1259-63, *Astroph. Space Sci.* **309**, 253 (2007), arXiv:astro-ph/0610139 [astro-ph].
- [14] A. Neronov and M. Ribordy, Neutrino signal from  $\gamma$ -ray loud binaries powered by high energy protons, *Phys. Rev. D* **79**, 043013 (2009), arXiv:0812.0306 [astro-ph].
- [15] A. M. Bykov, A. E. Petrov, M. E. Kalyashova, and S. V. Troitsky, PeV Photon and Neutrino Flares from Galactic Gamma-Ray Binaries, *ApJ* **921**, L10 (2021), arXiv:2110.11189 [astro-ph.HE].
- [16] G. Dubus, Gamma-ray binaries and related systems, *Astron. Astroph. Reviews* **21**, 64 (2013), arXiv:1307.7083 [astro-ph.HE].
- [17] H. Yoneda, K. Makishima, T. Enoto, D. Khangulyan, T. Matsumoto, and T. Takahashi, Sign of Hard-X-Ray Pulsation from the  $\gamma$ -Ray Binary System LS 5039, *Phys. Rev. Lett.* **125**, 111103 (2020), arXiv:2009.02075 [astro-ph.HE].
- [18] O. Kargaltsev, J. Hare, I. Volkov, and A. Lange, A Lack of 9 s Periodicity in the Follow-up NuSTAR Observation of LS 5039, *ApJ* **958**, 79 (2023), arXiv:2310.06810 [astro-ph.HE].
- [19] K. Makishima, N. Uchida, H. Yoneda, T. Enoto, and T. Takahashi, Further Evidence for the 9 s Pulsation in LS 5039 from NuSTAR and ASCA, *ApJ* **959**, 79 (2023), arXiv:2311.06473 [astro-ph.HE].
- [20] S.-S. Weng, L. Qian, B.-J. Wang, D. F. Torres, A. Pappitto, P. Jiang, R. Xu, J. Li, J.-Z. Yan, Q.-Z. Liu, M.-Y. Ge, and Q.-R. Yuan, Radio pulsations from a neutron star within the gamma-ray binary LS I +61° 303, *Nature Astronomy* **6**, 698 (2022), arXiv:2203.09423 [astro-ph.HE].
- [21] J. López-Miralles, S. E. Motta, S. Migliari, and F. Jaron, Rapid X-ray variability of the gamma-ray binary LS I +61°303, *MNRAS* **523**, 4282 (2023), arXiv:2305.18580 [astro-ph.HE].
- [22] Z. Cao, F. A. Aharonian, Q. An et al. Ultrahigh-energy photons up to 1.4 petaelectronvolts from 12  $\gamma$ -ray Galactic sources, *Nat* **594**, 33 (2021).
- [23] D. D. Dzhappuev, Y. Z. Afashokov, I. M. Dzaparova et al. Observation of Photons above 300 TeV Associated with a High-energy Neutrino from the Cygnus Region, *ApJ* **916**, L22 (2021), arXiv:2105.07242 [astro-ph.HE].
- [24] V. Bosch-Ramon and M. V. Barkov, Large-scale flow dynamics and radiation in pulsar  $\gamma$ -ray binaries, *A&A* **535**, A20 (2011), arXiv:1105.6236 [astro-ph.HE].
- [25] V. Bosch-Ramon, M. V. Barkov, D. Khangulyan, and M. Perucho, Simulations of stellar/pulsar-wind interaction along one full orbit, *A&A* **544**, A59 (2012), arXiv:1203.5528 [astro-ph.HE].
- [26] V. Bosch-Ramon, M. V. Barkov, and M. Perucho, Orbital evolution of colliding star and pulsar winds in 2D and 3D: effects of dimensionality, EoS, resolution, and grid size, *A&A* **577**, A89 (2015), arXiv:1411.7892 [astro-ph.HE].
- [27] G. Dubus, A. Lamberts, and S. Fromang, Modelling the high-energy emission from gamma-ray binaries using numerical relativistic hydrodynamics, *A&A* **581**, A27 (2015), arXiv:1505.01026 [astro-ph.HE].
- [28] V. Bosch-Ramon, M. V. Barkov, A. Mignone, and P. Bordas, HESS J0632+057: hydrodynamics and non-thermal emission, *MNRAS* **471**, L150 (2017), arXiv:1708.00066 [astro-ph.HE].
- [29] D. Huber, R. Kissmann, and O. Reimer, Relativistic fluid modelling of gamma-ray binaries. II. Application to LS 5039, *A&A* **649**, A71 (2021), arXiv:2103.00995 [astro-ph.HE].
- [30] J. H. Grunhut, G. A. Wade, C. Neiner, M. E. Oksala, V. Petit, E. Alecian, D. A. Bohlender, J. C. Bouret, H. F. Henrichs, G. A. J. Hussain, O. Kochukhov, and MiMeS Collaboration, The MiMeS survey of Magnetism in Massive Stars: magnetic analysis of the O-type stars, *MNRAS* **465**, 2432 (2017), arXiv:1610.07895 [astro-ph.SR].
- [31] M. E. Shultz, G. A. Wade, T. Rivinius, E. Alecian, C. Neiner, V. Petit, S. Owocki, A. ud-Doula, O. Kochukhov, D. Bohlender, Z. Keszthelyi, MiMeS Collaboration, and BinaMIcS Collaboration, The magnetic early B-type stars - III. A main-sequence magnetic, rotational, and magnetospheric biography, *MNRAS* **490**, 274 (2019), arXiv:1909.02530 [astro-ph.SR].
- [32] A. M. Bykov, A. E. Petrov, G. A. Ponomaryov, K. P. Levenfish, and M. Falanga, PeV proton acceleration in gamma-ray binaries, *Advances in Space Research* **74**, 4276 (2024), arXiv:2401.06271 [astro-ph.HE].
- [33] J. Casares, M. Ribó, I. Ribas, J. M. Paredes, J. Martí, and A. Herrero, A possible black hole in the  $\gamma$ -ray microquasar LS 5039, *MNRAS* **364**, 899 (2005), arXiv:astro-ph/0507549 [astro-ph].
- [34] W. C. G. Ho, C. Y. Ng, A. G. Lyne, B. W. Stappers, M. J. Coe, J. P. Halpern, T. J. Johnson, and I. A. Steele, Multi-wavelength monitoring and X-ray brightening of Be X-ray binary PSR J2032+4127/MT91 213 on its approach to periastron, *MNRAS* **464**, 1211 (2017), arXiv:1609.06328 [astro-ph.SR].
- [35] S. V. Bogovalov, D. V. Khangulyan, A. V. Koldoba, G. V. Ustyugova, and F. A. Aharonian, Modelling interaction of relativistic and non-relativistic winds in binary system PSR B1259-63/SS2883 - I. Hydrodynamical limit, *MNRAS* **387**, 63 (2008), arXiv:0710.1961 [astro-ph].
- [36] R. Klement, A. C. Carciofi, T. Rivinius, L. D. Matthews, R. G. Vieira, R. Ignace, J. E. Bjorkman, B. C. Mota, D. M. Faes, A. D. Bratcher, M. Curé, and S. Štefl, Revealing the structure of the outer disks of Be stars, *A&A* **601**, A74 (2017), arXiv:1703.07321 [astro-ph.SR].
- [37] F. C. Michel, Rotating Magnetospheres: an Exact 3-D Solution, *ApJ* **180**, L133 (1973).
- [38] Y. E. Lyubarsky, On the structure of the inner Crab Nebula, *MNRAS* **329**, L34 (2002).
- [39] M. C. Weisskopf, J. J. Hester, A. F. Tennant, R. F. Elsner, N. S. Schulz, H. L. Marshall, M. Karovska, J. S. Nichols, D. A. Swartz, J. J. Kolodziejczak, and S. L. O'Dell, Discovery of Spatial and Spectral Structure in the X-Ray Emission from the Crab Nebula, *ApJ* **536**, L81 (2000), arXiv:astro-ph/0003216 [astro-ph].

- [40] J. J. Hester, K. Mori, D. Burrows, J. S. Gallagher, J. R. Graham, M. Halverson, A. Kader, F. C. Michel, and P. Scowen, Hubble Space Telescope and Chandra Monitoring of the Crab Synchrotron Nebula, *ApJ* **577**, L49 (2002).
- [41] G. G. Pavlov, O. Y. Kargaltsev, D. Sanwal, and G. P. Garmire, Variability of the Vela Pulsar Wind Nebula Observed with Chandra, *ApJ* **554**, L189 (2001), arXiv:astro-ph/0104264 [astro-ph].
- [42] D. J. Helfand, E. V. Gotthelf, and J. P. Halpern, Vela Pulsar and Its Synchrotron Nebula, *ApJ* **556**, 380 (2001), arXiv:astro-ph/0007310 [astro-ph].
- [43] G. G. Pavlov, M. A. Teter, O. Kargaltsev, and D. Sanwal, The Variable Jet of the Vela Pulsar, *ApJ* **591**, 1157 (2003), arXiv:astro-ph/0305510 [astro-ph].
- [44] O. Kargaltsev, B. Cerutti, Y. Lyubarsky, and E. Striani, Pulsar-Wind Nebulae. Recent Progress in Observations and Theory, *Space Sci. Rev.* **191**, 391 (2015), arXiv:1507.03662 [astro-ph.HE].
- [45] S. S. Komissarov and Y. E. Lyubarsky, Synchrotron nebulae created by anisotropic magnetized pulsar winds, *MNRAS* **349**, 779 (2004).
- [46] L. Del Zanna, E. Amato, and N. Bucciantini, Axially symmetric relativistic MHD simulations of Pulsar Wind Nebulae in Supernova Remnants. On the origin of torus and jet-like features, *A&A* **421**, 1063 (2004), arXiv:astro-ph/0404355 [astro-ph].
- [47] N. F. Camus, S. S. Komissarov, N. Bucciantini, and P. A. Hughes, Observations of ‘wisps’ in magnetohydrodynamic simulations of the Crab Nebula, *MNRAS* **400**, 1241 (2009), arXiv:0907.3647 [astro-ph.HE].
- [48] O. Porth, S. S. Komissarov, and R. Keppens, Three-dimensional magnetohydrodynamic simulations of the Crab nebula, *MNRAS* **438**, 278 (2014), arXiv:1310.2531 [astro-ph.HE].
- [49] B. Olmi, L. Del Zanna, E. Amato, R. Bandiera, and N. Bucciantini, On the magnetohydrodynamic modelling of the Crab nebula radio emission, *MNRAS* **438**, 1518 (2014), arXiv:1310.8496 [astro-ph.HE].
- [50] B. Olmi, L. Del Zanna, E. Amato, N. Bucciantini, and A. Mignone, Multi-D magnetohydrodynamic modelling of pulsar wind nebulae: recent progress and open questions, *Journal of Plasma Physics* **82**, 635820601 (2016), arXiv:1610.07956 [astro-ph.HE].
- [51] R. Bühler and M. Giomi, The imprint of pulsar parameters on the morphology of Pulsar Wind Nebulae, *MNRAS* **462**, 2762 (2016), arXiv:1607.04277 [astro-ph.HE].
- [52] K. P. Levenfish, G. A. Ponomaryov, A. E. Petrov, A. M. Bykov, and A. M. Krassilchtchikov, Slow motion pulsar wind nebulae, in *Journal of Physics Conference Series*, *Journal of Physics Conference Series*, Vol. 2103 (IOP, 2021) p. 012020.
- [53] G. A. Ponomaryov, A. N. Fursov, S. S. Fateeva, K. P. Levenfish, A. E. Petrov, and A. M. Krassilchtchikov, On the Origin of Knots in the Vela Nebula, *Astronomy Letters* **49**, 65 (2023).
- [54] S. S. Komissarov and M. Lyutikov, On the origin of variable gamma-ray emission from the Crab nebula, *MNRAS* **414**, 2017 (2011), arXiv:1011.1800 [astro-ph.HE].
- [55] O. Porth, R. Buehler, B. Olmi, S. Komissarov, A. Lamberts, E. Amato, Y. Yuan, and A. Rudy, Modelling Jets, Tori and Flares in Pulsar Wind Nebulae, *Space Sci. Rev.* **207**, 137 (2017), arXiv:1703.05184 [astro-ph.HE].
- [56] E. Amato, The theory of Pulsar Wind Nebulae: recent progress, arXiv e-prints , arXiv:2001.04442 (2020), arXiv:2001.04442 [astro-ph.HE].
- [57] B. Olmi and N. Bucciantini, The Dawes Review 11: From young to old: The evolutionary path of Pulsar Wind Nebulae, *PASA* **40**, e007 (2023), arXiv:2301.12903 [astro-ph.HE].
- [58] G. A. Ponomaryov, K. P. Levenfish, and A. E. Petrov, Jet and counter-jet in transonic pulsar wind nebulae, in *Journal of Physics Conference Series*, *Journal of Physics Conference Series*, Vol. 2103 (IOP, 2021) p. 012021.
- [59] R. A. Chevalier and S. P. Reynolds, Pulsar Wind Nebulae with Thick Toroidal Structure, *ApJ* **740**, L26 (2011), arXiv:1109.1752 [astro-ph.HE].
- [60] S. S. Fateeva, K. P. Levenfish, G. A. Ponomaryov, A. E. Petrov, and A. N. Fursov, On the Nature of the Bar-Shaped X-ray Feature in the Lee Jet of the Vela Pulsar Wind Nebula, *Astronomy Letters* **49**, 56 (2023).
- [61] A. E. Petrov, K. P. Levenfish, and G. A. Ponomaryov, Reverberation of the Vela Pulsar Wind Nebula, *Astronomy Letters* **49**, 777 (2023).
- [62] O. Kargaltsev, G. G. Pavlov, D. Sanwal, and G. P. Garmire, The Vela Pulsar Wind Nebula Resolved with Chandra, in *Neutron Stars in Supernova Remnants*, *Astronomical Society of the Pacific Conference Series*, Vol. 271, edited by P. O. Slane and B. M. Gaensler (2002) p. 181.
- [63] M. Durant, O. Kargaltsev, G. G. Pavlov, J. Kropotina, and K. Levenfish, The Helical Jet of the Vela Pulsar, *ApJ* **763**, 72 (2013), arXiv:1211.0347 [astro-ph.HE].
- [64] A. M. Bykov, E. Amato, A. E. Petrov, A. M. Krassilchtchikov, and K. P. Levenfish, Pulsar Wind Nebulae with Bow Shocks: Non-thermal Radiation and Cosmic Ray Leptons, *Space Sci. Rev.* **207**, 235 (2017), arXiv:1705.00950 [astro-ph.HE].
- [65] D. M. A. Meyer, Z. Meliani, P. F. Velázquez, M. Pohl, and D. F. Torres, On the plerionic rectangular supernova remnants of static progenitors, *MNRAS* **527**, 5514 (2024), arXiv:2311.06817 [astro-ph.HE].
- [66] M. Lemoine, Magnetised turbulent plasmas as high-energy particle accelerators, arXiv e-prints , arXiv:2512.15239 (2025), arXiv:2512.15239 [astro-ph.HE].
- [67] M. Lemoine, V. Bresci, and L. Gremillet, Particle acceleration up to the synchrotron burn-off limit in relativistic magnetized turbulence, *Phys. Rev. D* **112**, 123028 (2025), arXiv:2509.06437 [astro-ph.HE].
- [68] The LHAASO Collaboration, Z. Cao, F. Aharonian et al. Cygnus X-3: A variable petaelectronvolt gamma-ray source, arXiv e-prints , arXiv:2512.16638 (2025), arXiv:2512.16638 [astro-ph.HE].
- [69] A. Mignone, G. Bodo, S. Massaglia, T. Matsakos, O. Tesileanu, C. Zanni, and A. Ferrari, PLUTO: A Numerical Code for Computational Astrophysics, *ApJS* **170**, 228 (2007), arXiv:astro-ph/0701854 [astro-ph].
- [70] Y. E. Lyubarsky, The termination shock in a striped pulsar wind, *MNRAS* **345**, 153 (2003), arXiv:astro-ph/0306435 [astro-ph].
- [71] S. S. Komissarov, Magnetic dissipation in the Crab nebula, *MNRAS* **428**, 2459 (2013), arXiv:1207.3192 [astro-ph.HE].
- [72] B. Cerutti, A. A. Philippov, and G. Dubus, Dissipation of the striped pulsar wind and non-thermal particle acceleration: 3D PIC simulations, *A&A* **642**, A204 (2020), arXiv:2008.11462 [astro-ph.HE].